

Sparse inpainting and isotropy

**Stephen M. Feeney,^a Domenico Marinucci,^b Jason D. McEwen,^{a,c}
Hiranya V. Peiris^{a,d} Benjamin D. Wandelt^{d,e,f,g} and Valentina
Cammara^b**

^aDepartment of Physics and Astronomy, University College London, London WC1E 6BT, UK

^bDepartment of Mathematics, University of Rome Tor Vergata, via della Ricerca Scientifica 1, 00133 Roma, Italy

^cMullard Space Science Laboratory (MSSL), University College London, Surrey RH5 6NT, UK

^dKavli Institute for Theoretical Physics, Kohn Hall, University of California, Santa Barbara, CA 93106, USA

^eInstitut d'Astrophysique de Paris, UMR 7095, CNRS - Université Pierre et Marie Curie (Univ Paris 06), 98 bis blvd Arago, 75014 Paris, France

^fSorbonne Université, Institut Lagrange de Paris (ILP), 98 bis bd Arago, 75014 Paris, France

^gDepartments of Physics and Astronomy, University of Illinois at Urbana-Champaign, Urbana, IL 61801, USA

E-mail: s.feeney@imperial.ac.uk

Abstract. Sparse inpainting techniques are gaining in popularity as a tool for cosmological data analysis, in particular for handling data which present masked regions and missing observations. We investigate here the relationship between sparse inpainting techniques using the spherical harmonic basis as a dictionary and the isotropy properties of cosmological maps, as for instance those arising from cosmic microwave background (CMB) experiments. In particular, we investigate the possibility that inpainted maps may exhibit anisotropies in the behaviour of higher-order angular polyspectra. We provide analytic computations and simulations of inpainted maps for a Gaussian isotropic model of CMB data, suggesting that the resulting angular trispectrum may exhibit small but non-negligible deviations from isotropy.

Contents

| | | |
|----------|--|-----------|
| 1 | Introduction | 1 |
| 2 | Sparse Inpainting | 2 |
| 3 | Independent Coefficients, Gaussianity and Isotropy | 5 |
| 4 | Analytic Computations and Simulations | 7 |
| 5 | Conclusions | 11 |
| A | The Laplacian trispectrum for the quadrupole and the octupole | 14 |

1 Introduction

Sparse inpainting techniques are becoming widespread tools for cosmic microwave background (CMB) data analysis. The reasons for their popularity are easily understood: on one hand these techniques belong to the rich framework of convex optimization procedures, and are related to deep and elegant mathematical results on compressive sensing (e.g., refs. [1–6]); on the other hand they address some important issues in practical cosmological data analysis, e.g., dealing with masked regions and missing observations. Consequently, inpainting techniques on the sphere [5–10] have now found successful applications for many astrophysical problems (see, e.g., refs. [7, 11, 12] and references therein).

Given the utility of these approaches for modern cosmological data analysis, it is important to investigate their properties from many different points of view. In particular, we shall be concerned here with the relationship between inpainting techniques and isotropy: we shall investigate whether inpainted maps retain the same isotropy properties as the input random fields from which they are derived. We shall show that, in principle, inpainting can produce anisotropies in CMB-like maps, in the form of a small modulation of the angular trispectrum. For brevity’s sake, we consider only the direct application of sparse inpainting techniques to low- ℓ CMB-only maps. Although extra factors, such as instrumental noise and beams and variable sky coverage, are present in more realistic scenarios, we conjecture that they will not substantially affect the core conclusions of this paper; we leave further investigation on this point to future research.

Our basic arguments can be summarized as follows. To understand the relationship between inpainting and isotropy, it can be convenient to recognize sparse inpainting with a spherical harmonic dictionary as operationally equivalent to maximizing a Bayesian posterior distribution assuming a Laplacian prior on the spherical harmonic coefficients $a_{\ell m}$. Earlier results from ref. [13] (see also refs. [14–16]) have shown that a random field generated by sampling such independent non-Gaussian coefficients is necessarily anisotropic. We demonstrate that the trispectrum of such a field exhibits a modulated behavior, containing a maximum at the North Pole and oscillations whose pattern can be analytically derived. Of course, the distribution of maximum *a posteriori* estimates is, in general, different from the law of the input prior; it is natural, however, to conjecture that the trispectrum of inpainted maps will at least partially inherit these anisotropic features. This conjecture is indeed confirmed by

our simulations, where CMB-like Gaussian isotropic maps are generated at low resolution, masked, and then inpainted: their trispectra contain a similar pattern to that analytically derived from the theoretical considerations, although with a smaller absolute amplitude.¹ It should be noted that our arguments and results apply only to sparse inpainting using the spherical harmonics as a dictionary, as proposed in ref. [8]; other dictionary choices, such as wavelets, may be free from such issues.

As was previously mentioned, the simulations are performed in somewhat idealized circumstances – namely at low band-limit (maximum harmonic mode $\ell_{\max} = 10$) and in the absence of noise or an instrumental beam – to ensure speed of calculation and clarity of results. A large sky cut is used to demonstrate the main result; a more moderate sky cut has also been shown to produce similar effects. Further investigations under more realistic conditions are left as an avenue for further research. We note that the trispectrum modulations for $\ell = 2$ and $\ell = 3$ exhibit qualitatively the same pattern; this could produce a spurious correlation between multipoles which are actually independent.

It is important to stress that we do not, by any means, view this paper as part of the long-standing debate between Bayesian and frequentist approaches in astrophysical data analysis; the authors of this paper have rather different points of view on these foundational issues. The Bayesian interpretation of inpainting techniques is introduced here merely as a heuristic rationale to motivate the investigation of the expected sample properties of inpainted maps: these properties are then considered in a setting which can be viewed as purely frequentist, i.e., by deriving analytically, and then supporting by simulations, the expected modifications of a standard trispectrum estimator defined on the inpainted maps. It would be possible, in principle, to correct the trispectrum modifications that result, but this is likely to be very demanding from the computational point of view.

The structure of the paper is as follows: in Sect. 2, we review convex regularization techniques and their relationship to Laplacian priors; in Sect. 3 we review earlier results from refs. [13, 14] on the relationship between Gaussianity, independent Fourier coefficients and isotropy; in Sect. 4 we present our simulations to support the findings of Sect. 3; concluding remarks are made in Sect. 5. Most analytic computations are collected in Appendix A.

2 Sparse Inpainting

It is well-known that sparse inpainting can be viewed as maximum *a posteriori* (MAP) estimation under a Laplacian prior (e.g., ref. [17]). In this section, we make the association explicit in the context of signals defined on the sphere, while also making a comparison to Wiener filtering.

Let us model the observed spatial data \mathbf{d} by

$$\mathbf{d} = \mathbf{Y}\mathbf{a} + \mathbf{n} ,$$

where \mathbf{Y} is the matrix with columns given by the spherical harmonic functions $Y_{\ell m}$ evaluated at the locations of the observed data, \mathbf{a} is the vector of associated harmonic coefficients $a_{\ell m}$, and \mathbf{n} is the noise on the measured spatial data. Assuming Gaussian noise with covariance $\mathbf{N} = \mathbb{E}(\mathbf{n}\mathbf{n}^\dagger)$, where $\mathbb{E}(\cdot)$ denotes expectation and \cdot^\dagger denotes the Hermitian transpose, the likelihood of the data is

$$P(\mathbf{d} | \mathbf{a}) \propto \exp(-\chi^2/2),$$

¹The Fortran code used to produce and inpaint these simulations is available for download from <http://zuserver2.star.ucl.ac.uk/~smf/code.html>.

where

$$\chi^2 = (\mathbf{d} - \mathbf{Y}\mathbf{a})^\dagger \mathbf{N}^{-1} (\mathbf{d} - \mathbf{Y}\mathbf{a}) .$$

The posterior distribution of the harmonic coefficients \mathbf{a} is then given by

$$P(\mathbf{a} | \mathbf{d}) \propto P(\mathbf{d} | \mathbf{a}) P(\mathbf{a}) .$$

We consider MAP estimates of the $a_{\ell m}$ s.² Firstly, assume the Gaussian prior distribution on the harmonic coefficients

$$P_{\text{Gauss}}(\mathbf{a}) \propto \exp(-\mathbf{a}^\dagger \mathbf{C}^{-1} \mathbf{a} / 2) ,$$

with covariance $\mathbf{C} = \mathbb{E}(\mathbf{a}\mathbf{a}^\dagger)$. This is a well-motivated physical prior for the CMB anisotropies, since it is well-known that, to first approximation, the primordial perturbations from inflation that are thought to have sourced these anisotropies are Gaussian. The MAP estimator under this prior corresponds to the usual Wiener filtering approach to inpainting (e.g., refs. [20–23]), i.e., recovering harmonic components from incomplete sky data, where the $a_{\ell m}$ s are given by the solution to the optimization problem

$$\hat{\mathbf{a}}_{\text{Wiener}} = \arg \min_{\mathbf{a}} (\mathbf{a}^\dagger \mathbf{C}^{-1} \mathbf{a} + \chi^2) ,$$

where the minimization is with respect to \mathbf{a} . This optimization problem can be solved analytically to give

$$\hat{\mathbf{a}}_{\text{Wiener}} = (\mathbf{Y}^\dagger \mathbf{N}^{-1} \mathbf{Y} + \mathbf{C}^{-1})^{-1} \mathbf{Y}^\dagger \mathbf{N}^{-1} \mathbf{d} .$$

Secondly, consider an alternative prior where each $a_{\ell m}$ is independent and Laplacian-distributed:

$$P(\mathbf{a}) = \prod_{\ell m} P_{\text{Laplacian}}(a_{\ell m}) \propto \exp(-\beta \|\mathbf{a}\|_1)$$

for scale parameter β , where we recall that the ℓ_1 norm of a vector is given by the sum of the absolute values of its entries, i.e., $\|\mathbf{a}\|_1 = \sum_{\ell m} |a_{\ell m}|$. The MAP estimator corresponding to this prior is thus recovered by solving the optimization problem

$$\hat{\mathbf{a}}_{\text{Laplacian}} = \arg \min_{\mathbf{a}} (\beta \|\mathbf{a}\|_1 + \chi^2 / 2) .$$

For the case of isotropic white noise, $\mathbf{N} = \sigma^2 \mathbb{I}$, where \mathbb{I} is the identity, the optimization problem may be rewritten

$$\hat{\mathbf{a}}_{\text{Laplacian}} = \arg \min_{\mathbf{a}} (\lambda \|\mathbf{a}\|_1 + \|\mathbf{d} - \mathbf{Y}\mathbf{a}\|_2^2) , \quad (2.1)$$

for $\lambda = 2\beta\sigma^2 > 0$, which acts as a regularization parameter, trading off sparsity against data fidelity. This is exactly the optimization problem described in ref. [9], eqns. (4-6), and is known as an *unconstrained* optimization, as a single object function (given by the sum of two terms) is optimized in the absence of any additional constraints.

Alternatively, *constrained* problems are sometimes considered, e.g.,

$$\hat{\mathbf{a}} = \arg \min_{\mathbf{a}} \|\mathbf{a}\|_1 \text{ such that } \mathbf{d} = \mathbf{Y}\mathbf{a} , \quad (2.2)$$

²Alternatively, sampling methods can be used to recover the full posterior distribution $P(\mathbf{a} | \mathbf{d})$ (e.g. refs. [18, 19]).

avoiding the need to choose a regularization parameter λ .³ This is the problem solved by the sparse inpainting algorithm described in Appendix B of ref. [8] and implemented here. The unconstrained and constrained problems are subtly different, but the unconstrained problem can nevertheless be used to gain insight (via its Bayesian interpretation) into the constrained problem (indeed, this intuition is born out in the analytic and simulated results presented subsequently).

We remark that viewing sparse inpainting as MAP estimation under a Laplacian prior is only one possible Bayesian interpretation. It has been shown by ref. [17] that, for white Gaussian noise, the Bayesian minimum mean-square error (MMSE) estimator for any prior is a solution to the penalized least-squares optimization problem with a suitable penalty function. Nevertheless, viewing sparse inpainting as MAP estimation under a Laplacian prior is indeed a valid interpretation; furthermore, in the case of a Gaussian prior, the MAP and MMSE estimators are equivalent.

We also remark that it is possible to consider two alternative implementation schemes for the optimization problems in eqns. (2.1) and (2.2), according to the different definitions we can take for the ℓ_1 norm. In particular, one can either define

$$\|\mathbf{a}\|_1 = \sum_{\ell m} |\Re a_{\ell m}| + |\Im a_{\ell m}| \quad (2.4)$$

or

$$\|\mathbf{a}\|_1 = \sum_{\ell m} \sqrt{(\Re a_{\ell m})^2 + (\Im a_{\ell m})^2}; \quad (2.5)$$

the former is the ℓ_1 norm of the separate real and imaginary components of the complex $a_{\ell m}$ s, whereas the latter is the ℓ_1 norm of the magnitude of the complex $a_{\ell m}$ s. We therefore refer to inpainting based on eqn. (2.4) as *separate* sparse inpainting, and that based on eqn. (2.5) as *joint* sparse inpainting. The analytic computations in Appendix A are based on eqn. (2.4), while the simulations cover both cases.

The constrained problem, eqn. (2.2), can be solved by an iterative algorithm based on Douglas-Rachford splitting [8, 24, 25]. Each iteration of this algorithm consists of two steps. In the first step, the data constraint is applied to the latest estimate of the $a_{\ell m}$ s, denoted \mathbf{a}^n , using a projection operator:

$$\mathbf{a}^{n+\frac{1}{2}} = \text{Proj}_{\{\mathbf{a}:\mathbf{d}=\mathbf{Y}\mathbf{a}\}}(\mathbf{a}^n). \quad (2.6)$$

The projection operator creates a map from the \mathbf{a}^n , sets the unmasked pixels of this map to their observed values, \mathbf{d} , and returns the spherical harmonic coefficients of this constrained map, $\mathbf{a}^{n+\frac{1}{2}}$. In the second step of each iteration, the sparsity prior is applied to the constrained harmonic coefficients. Mathematically, this operation takes the form

$$\mathbf{a}^{n+1} = \mathbf{a}^n + \left(\text{sgn}(2\mathbf{a}^{n+\frac{1}{2}} - \mathbf{a}^n) \max(0, |2\mathbf{a}^{n+\frac{1}{2}} - \mathbf{a}^n| - \lambda) \right) - \mathbf{a}^{n+\frac{1}{2}}, \quad (2.7)$$

where $\lambda > 0$ corresponds again to a weight applied to $\|\mathbf{a}\|_1$ and governs the rate of convergence of the algorithm⁴ but, in theory, does not affect the solution. Roughly speaking, this operation

³An alternative constrained problem can also be considered:

$$\hat{\mathbf{a}} = \arg \min_{\mathbf{a}} \|\mathbf{a}\|_1 \text{ such that } \|\mathbf{d} - \mathbf{Y}\mathbf{a}\|_2^2 \leq \epsilon^2, \quad (2.3)$$

where ϵ is chosen from the statistical properties of the noise in the observations (e.g., ref. [10]).

⁴“Rate” here is taken to mean the overall computation speed, not the asymptotic complexity of the algorithm (e.g., $\mathcal{O}(n^x)$). Changing λ changes the constant of proportionality relating the complexity to the computation speed.

sets the constrained $a_{\ell m}$ s with magnitudes less than λ to zero, and reduces the magnitudes of the others by λ , thus promoting a sparse solution. We choose λ to be unity, and verify using both simulations with varying λ and convergence checks (discussed in further detail in Sect. 4) that the precise value chosen is unimportant. We initialize the algorithm with a warm start to speed up convergence, taking the cut-sky $a_{\ell m}$ s as the starting point, \mathbf{a}^0 ; again, we verify through simulations that the precise choice of \mathbf{a}^0 does not affect the results.

The sequence of $a_{\ell m}$ s produced by the *first* step, eqn. (2.6), converges to a global minimizer of eqn. (2.2) [24]. Applying this algorithm as written (i.e., to vectors of complex spherical harmonic coefficients) therefore implements joint sparse inpainting; as eqn. (2.4) is equivalent to the ℓ_1 norm of the *real* $a_{\ell m}$ s, we can perform separate sparse inpainting by replacing the complex $a_{\ell m}$ s in eqns. (2.6) and (2.7) with their real counterparts.

The interplay between the two steps in the Douglas-Rachford algorithm is illustrated in Fig. 1. In this demonstration, a Gaussian CMB map with $\ell_{\max} = 10$ (Panel (a)) is masked with a 20 degree sky cut and inpainted using the joint sparse inpainting algorithm. In Panel (b) we show the one-norm of the $a_{\ell m}$ s, $\|\mathbf{a}\|_1$, and the square of the reconstruction error, $\|\mathbf{d} - \mathbf{Y}\mathbf{a}\|_2^2$, each normalized by their maximum value, at each step of each iteration. It is clearly seen that the algorithm alternates between promoting data fidelity (at each “half” step) and sparsity (at each “full” step). Panels (c) and (d) show the inpainted map after the final data-constraint step and the final sparsity step: the fidelity of the reconstruction is higher in Panel (c), and the $a_{\ell m}$ s have lower magnitudes in Panel (d).

3 Independent Coefficients, Gaussianity and Isotropy

In this section we shall point out that independent, non-Gaussian spherical harmonic coefficients necessarily correspond to an anisotropic random field. It is proved by refs. [13, 14] (see also ref. [15], Ch. 5, and ref. [16]) that, for an isotropic random field, the $a_{\ell m}$ coefficients can be independent if and only if they are Gaussian. While we do not reproduce the full proof of this statement here, it is simple to provide a heuristic explanation. It is indeed well known that, under isotropy,

$$\mathbf{a}_\ell \stackrel{d}{=} D_\ell(g) \mathbf{a}_\ell ,$$

where $g \in \text{SO}(3)$ is any rotation in \mathbb{R}^3 , $D_\ell(g)$ represents Wigner’s D -matrices (see, e.g., refs. [15, 26]), \mathbf{a}_ℓ represents the vector of spherical harmonic coefficients at any multipole ℓ , and $\stackrel{d}{=}$ denotes equality in distribution, i.e., the left- and right-hand sides have the same probability law. This identity must hold for any change of coordinates under isotropy, but it is easily seen to be violated by non-Gaussian independent priors. For instance, if we take \mathbf{a}_ℓ to have independent exponential entries, then the components of $D_\ell(g)\mathbf{a}_\ell$ will be represented by linear combinations of these exponentials; the latter are neither independent nor exponentially distributed, for general choices of the rotation g .

To give a more concrete example, let us assume we have generated a random field by sampling independent Laplacian-distributed $a_{\ell m}$ s, which we take to have unit variance for notational simplicity (see Appendix A). Consider the multipole component

$$T_\ell(x) = \sum_m a_{\ell m} Y_{\ell m}(x) ,$$

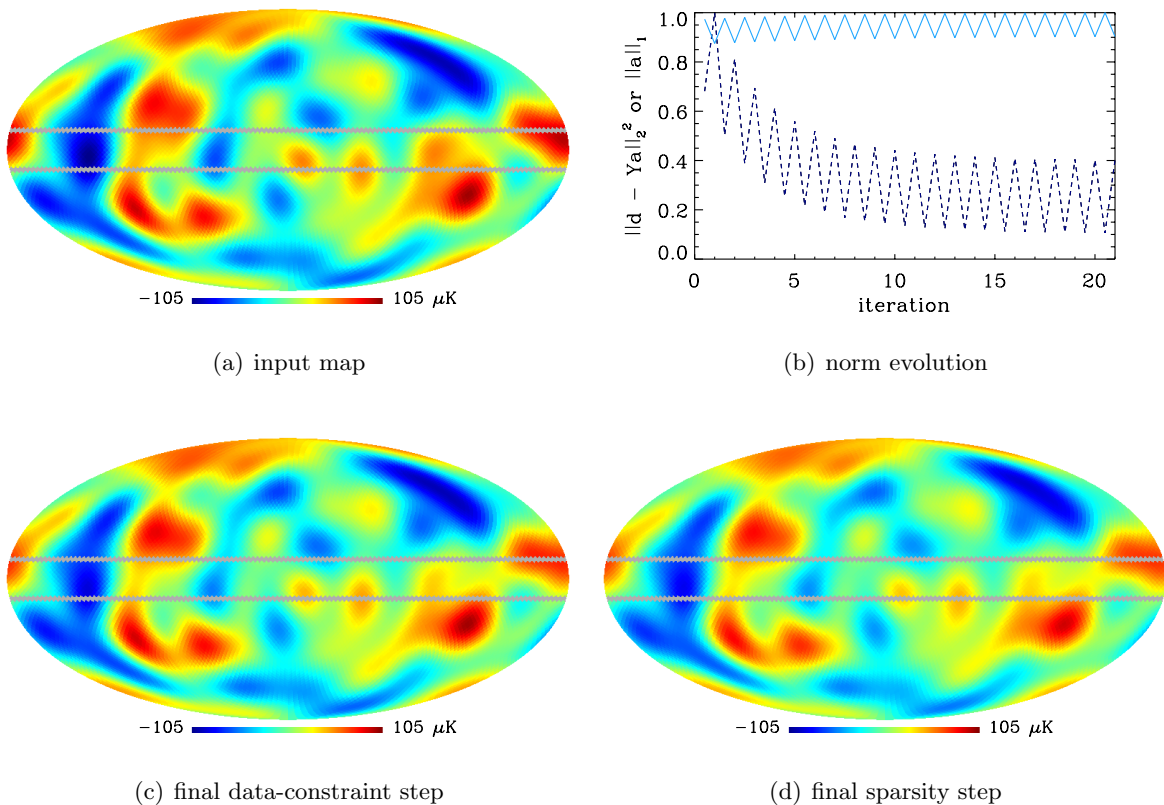


Figure 1. Illustration of the sparse inpainting procedure. A Gaussian CMB realisation with $\ell_{\max} = 10$ (top left) is masked with a 20 degree sky cut (indicated in grey) and inpainted using the Douglas-Rachford algorithm. The evolution of the one-norm of the $a_{\ell m}$ s, $\|\mathbf{a}\|_1$, (light blue, solid) and the squared reconstruction error, $\|\mathbf{d} - \mathbf{Y}\mathbf{a}\|_2^2$ (dark-blue, dashed), are plotted in the top right, clearly showing the interplay between the two steps. The inpainted map is shown after the final data constraint step (bottom left) and the final sparsity step (bottom right).

with $x \in \mathbb{S}^2$. Because the spherical harmonics $Y_{\ell m}$ are identically zero for $m \neq 0$ at the North Pole $N = (0, 0, 1)$, we have immediately

$$T_\ell(N) = a_{\ell 0} \sqrt{\frac{2\ell + 1}{4\pi}},$$

meaning that at the North Pole $T_\ell(x)$ has itself a Laplacian distribution. However, for different directions in the sky the law of $T_\ell(x)$ will be given by linear combinations of the $a_{\ell m}$ s weighted by spherical harmonics, and as such it will be much closer to Gaussianity due to a central-limit theorem (CLT)-like argument. For instance, the expected value of $T_\ell^4(x)$ (i.e., the trispectrum) will not be invariant to rotations, and isotropy will consequently be violated. It is a matter of simple algebra to show that

$$\mathbb{E}(T_\ell^2(x)) = \langle T_\ell^2(x) \rangle = \sum_m |Y_{\ell m}(x)|^2 \frac{1}{\sqrt{2}} \int_{-\infty}^{\infty} u^2 e^{-\sqrt{2}|u|} du = \frac{2\ell + 1}{4\pi},$$

which shows that the variance of these multipole components is indeed constant across the sky, so isotropy is not violated at the second order level. However, for the fourth-moment we

obtain

$$\mathbb{E}(T_\ell^4(N)) = \left\{ \sqrt{\frac{2\ell+1}{4\pi}} \right\}^4 \mathbb{E}(a_{\ell 0}^4) = \left\{ \sqrt{\frac{2\ell+1}{4\pi}} \right\}^4 \frac{1}{\sqrt{2}} \int_{-\infty}^{\infty} u^4 e^{-\sqrt{2}|u|} du = 6 \left\{ \sqrt{\frac{2\ell+1}{4\pi}} \right\}^4 ,$$

so that, normalizing the variance to unity,

$$\frac{\mathbb{E}(T_\ell^4(N))}{[\mathbb{E}(T_\ell^2(N))]^2} = 6 . \quad (3.1)$$

More generally, for an arbitrary direction $x \in S^2$ we have

$$\begin{aligned} \mathbb{E}(T_\ell^4(x)) &= \mathbb{E} \left\{ \sum_m a_{\ell m} Y_{\ell m}(x) \right\}^4 \\ &= \sum_m \mathbb{E}(a_{\ell m}^4) |Y_{\ell m}(x)|^4 + 3 \sum_{m, m'} \mathbb{E}(a_{\ell m}^2) |Y_{\ell m}(x)|^2 \mathbb{E}(a_{\ell m'}^2) |Y_{\ell m'}(x)|^2 \\ &= 6 \sum_m |Y_{\ell m}(x)|^4 + 3 \sum_{m \neq m'} |Y_{\ell m}(x)|^2 |Y_{\ell m'}(x)|^2 . \end{aligned}$$

This quantity is clearly not constant for different values of x , whence the anisotropic behaviour of fourth-order moments (trispectra) is evident. In the next section, we provide more detailed analysis on this same issue, and demonstrate that features present in the trispectrum of pure-Laplacian random fields can be inherited by sparsely inpainted Gaussian CMB maps.

4 Analytic Computations and Simulations

In Appendix A we provide analytic expressions for the trispectrum of the quadrupole and the octupole in the case of independent, Laplacian-distributed random spherical harmonic coefficients $a_{\ell m}$. These expressions can be plotted on the meridian with longitude $\varphi = 0$, showing a clear modulation over the sky with maxima at the North and South Poles and oscillatory behaviour between: see Fig. 2. The quantity plotted here is the excess kurtosis evaluated on a grid of colatitude θ , which is related to eqn. (A.1) ($\ell = 2$) and eqn. (A.2) ($\ell = 3$) given in Appendix A via $\kappa = \mathbb{E}(T_\ell^4(\theta, 0)) / [\mathbb{E}(T_\ell^2(\theta, 0))]^2 - 3$.

As shown by our simulations below, this pattern can remain in Gaussian inpainted maps, thus introducing a small but non-negligible deviation from isotropy. To demonstrate this effect, we have generated 100 000 Gaussian isotropic maps at low resolution ($\ell_{\max} = 10$,⁵ $N_{\text{side}} = 32$). We mask a 60-degree-wide azimuthally-symmetric strip, centered on the equator, and inpaint the masked maps using the ℓ_1 -minimization procedure described in Sect. 2, employing both joint and separate sparsity priors. To ensure that a satisfactory solution to the constrained optimization problem (eqn. 2.2) is found for each map, we augment this procedure with a convergence check, as opposed to running for a set number of iterations. The algorithm is taken to have converged when the energy of the update to the inpainted

⁵The results of ref. [8] were computed using a higher band-limit of 50. Due to the large number of simulations required to demonstrate our results, we use $\ell_{\max} = 10$; we have verified that our results do not change when ℓ_{\max} is set to 50.

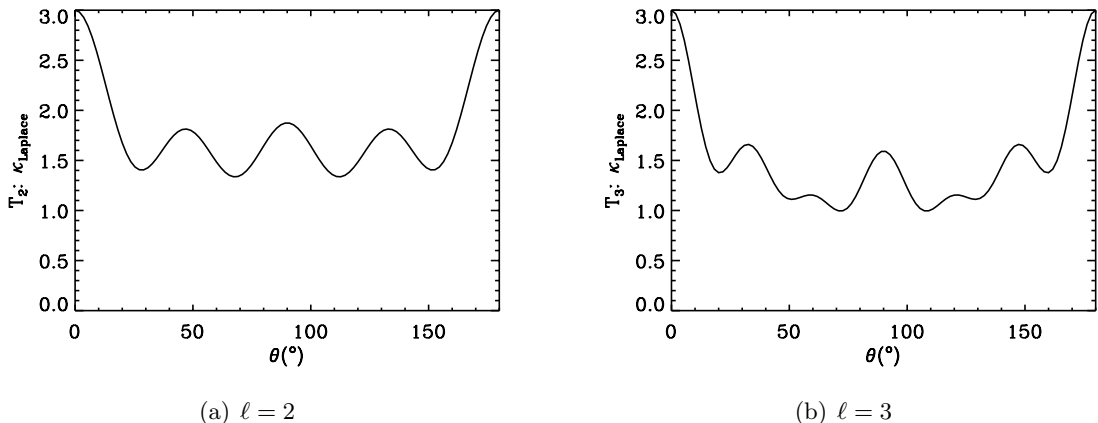


Figure 2. Analytic Laplacian trispectrum as derived in Appendix A for the separate inpainting optimization scheme. We plot the excess kurtosis evaluated on a grid of colatitude θ , which is related to eqn. (A.1) ($\ell = 2$) and eqn. (A.2) ($\ell = 3$) via $\kappa = \mathbb{E}(T_\ell^4(\theta, 0)) / [\mathbb{E}(T_\ell^2(\theta, 0))]^2 - 3$.

$a_{\ell m s}$ at the n^{th} iteration, $\Delta \mathbf{a}^n$, is less than 0.1% of the energy of the inpainted $a_{\ell m s}$ themselves, i.e., when $\|\Delta \mathbf{a}^n\|_2 / \|\mathbf{a}^n\|_2 \leq 0.001$. If the convergence criterion is not satisfied within 150 iterations, we replace the map with a new random draw and repeat the masking and inpainting procedure. To gain insight into the performance of the inpainting procedure, we also calculate two other estimates of the full-sky $a_{\ell m s}$ for each of the 100 000 input maps, namely the cut-sky $a_{\ell m s}$ and the Wiener-filtered $a_{\ell m s}$. Finally, we evaluate the Monte Carlo averages for the trispectrum of the quadrupole and octupole for all four estimators in the form of the excess kurtosis along the $\varphi = 0$ meridian: $\kappa = \mathbb{E}(T_\ell^4(\theta, 0)) / [\mathbb{E}(T_\ell^2(\theta, 0))]^2 - 3$.

Our primary results are shown in Figs. 3, 4 and 5. The main finding is summarized by the solid black line in each plot: this is the trispectrum of the ensemble of inpainted maps (for $\ell = 2$ or $\ell = 3$), evaluated on a grid of colatitude θ . Also plotted are the trispectrum of the input Gaussian maps (dashed), and the one-sigma Monte Carlo sampling error on the trispectrum of the Gaussian maps, for 100 000 realizations. The trispectrum of the input maps is clearly consistent with Gaussianity and isotropy. On the other hand, it is quite evident from Figs. 3 and 4 that the trispectra of the sparse-inpainted maps are clearly significantly different from zero everywhere, and exhibit similar qualitative features as those illustrated in our analytic computations (c.f. Fig. 2): namely a clear anisotropic modulation over the meridian, with peaks at the North Pole for both the quadrupole and octupole. Note that the maximum anisotropy appears at the points furthest from the mask: hence the effect we are describing cannot simply be confined within the inpainted portion of the map.

This anisotropy is not present in the maps generated using the other $a_{\ell m}$ estimators. Fig. 5 shows no significant non-Gaussianity nor anisotropy for either the cut-sky or Wiener-filtered maps: the fluctuations are fully within the Monte Carlo one-sigma confidence bounds, represented by the dotted lines. As far as the cut-sky maps are concerned, this may at first sight seem somewhat surprising, given that the mask does introduce anisotropic behavior; however, this can be explained by noting that the anisotropy in the variance is fully taken into account, because the kurtosis is itself normalized by the Monte Carlo second moment at the corresponding colatitude.

We recall that the results are obtained with a sky cut masking a 60 degree strip, i.e.

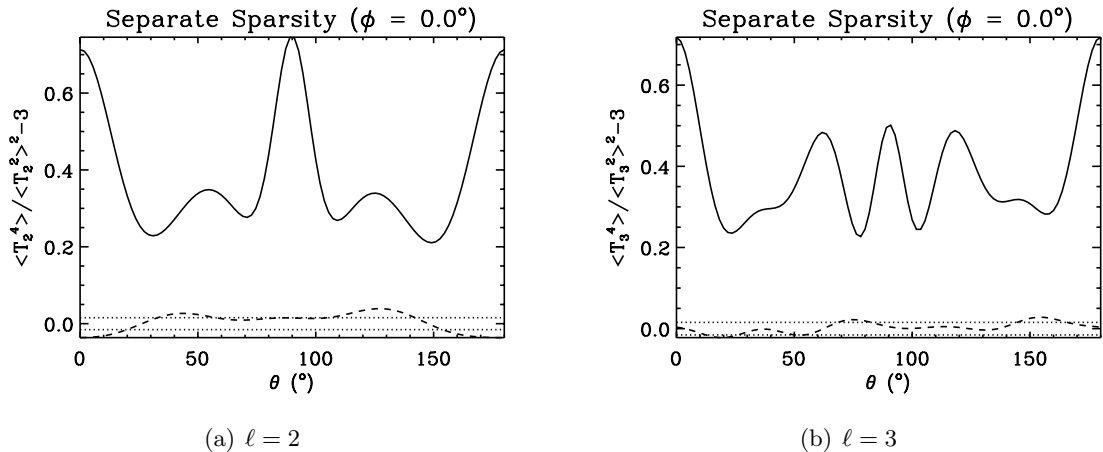


Figure 3. Simulated inpainted trispectrum, assuming *separate* sparsity. The trispectrum of the ensemble of inpainted maps is shown as a function of colatitude θ by the solid black line; the trispectrum of the input Gaussian maps is shown by the dashed line. The dotted lines show the one-sigma Monte Carlo sampling error on the trispectrum of the 100 000 Gaussian realizations, which are manifestly consistent with Gaussianity and isotropy. The trispectrum of the inpainted maps is clearly significantly different from zero everywhere, and is similar to the Laplacian trispectrum analytically derived in Appendix A and plotted in Fig. 2. The magnitude of the anisotropic signal for a given ℓ -mode is around 25% of the Gaussian expected value. Results are obtained using input maps with $\ell_{\max} = 10$, and cutting a 60 degree region, i.e., one half of the sky.

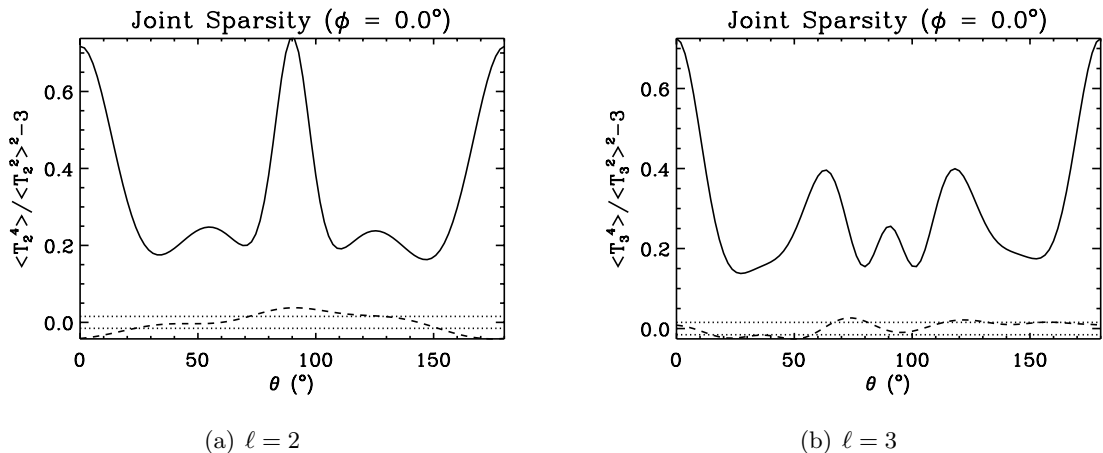


Figure 4. Simulated inpainted trispectrum, assuming *joint* sparsity, using the same line conventions as Fig. 3. The trispectrum of the inpainted maps is, again, clearly significantly different from zero everywhere; the precise shape of the trispectrum of the inpainted maps is slightly different to the separate-sparsity case, but the magnitude of the anisotropic signal for a given ℓ -mode remains $\sim 25\%$ of the Gaussian expected value. As before, results are obtained using input maps with $\ell_{\max} = 10$, and cutting a 60° region, i.e., one half of the sky.

half of the sky; larger than those used in typical CMB analyses. We have therefore repeated the analysis using a smaller sky cut, removing only a 20 degree strip of sky, and have found a similar pattern in the trispectra of the inpainted maps, albeit at reduced amplitude. The magnitude of the anisotropic signal for a given ℓ -mode is around 25% of the expected Gaussian

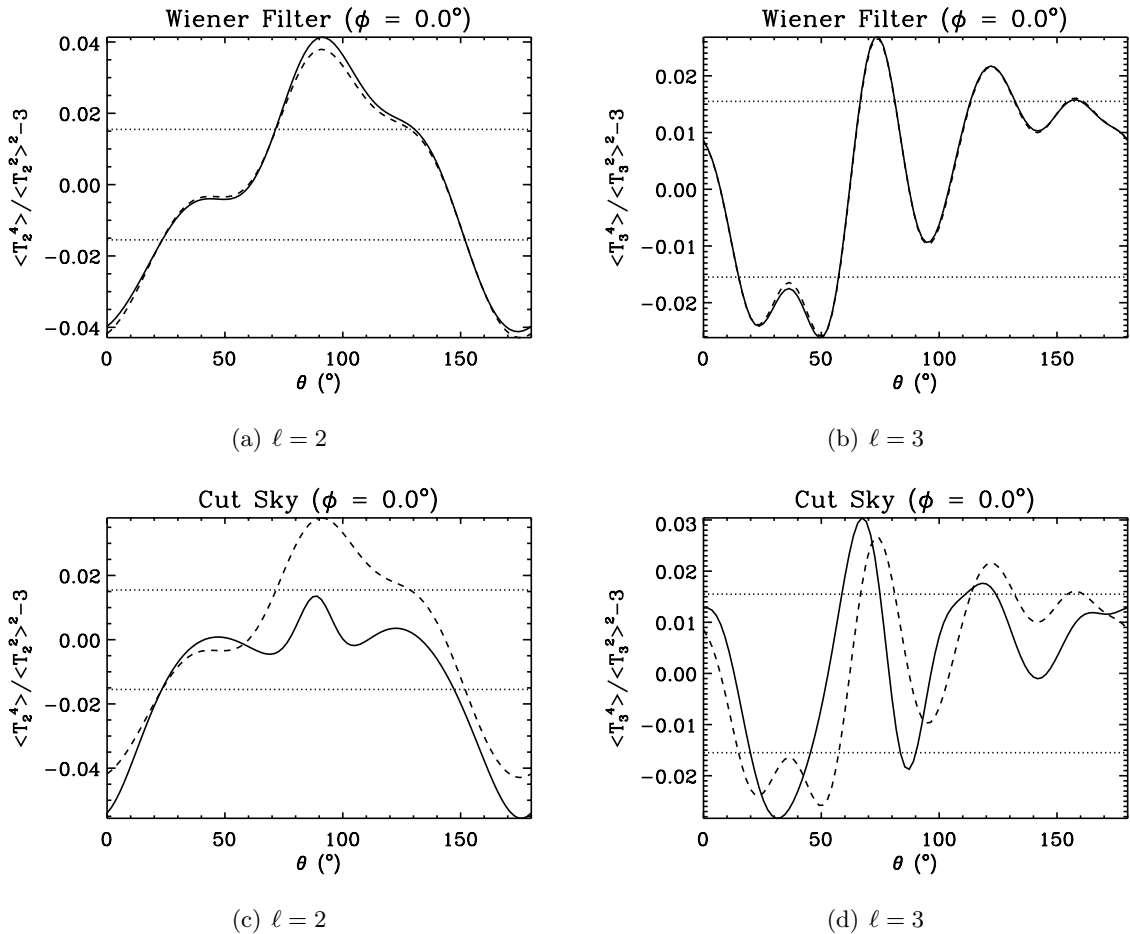


Figure 5. Trispectra of Wiener-filtered (top) and cut-sky (bottom) maps, using the same line conventions as Fig. 3. Neither the Wiener-filtered nor cut-sky maps show any significant deviation from isotropy.

value for the 60 degree sky cut, and 3–4% for a smaller sky cut of 20 degrees.⁶ Nevertheless, the effect is highly significant for the present simulations: the signal is several times larger than the Monte Carlo variance. Note also that, while the effect for a given multipole configuration is small, the cardinality of different trispectra configurations at *Planck* [27] resolution is very large. Thus, it is possible that statistics can be formulated that will spuriously detect broken statistical isotropy in inpainted maps due to the effect described in this work; for instance, an anisotropic feature may be mistakenly confused with an unexpected stochastic dependence. Further investigations are hence needed to assess the cumulative impact for the statistical analysis of a complete data set.

We also reiterate that the results are obtained using maps with a low band-limit ($\ell_{\max} = 10$), due to the large number of simulations required to reduce the sampling error on the kurtosis. To provide some hints on the behaviour of trispectra at higher multipoles, we have repeated the simulation-inpainting procedure using a higher band-limit of $\ell_{\max} = 50$,

⁶Note that it is also possible to terminate the inpainting procedure after the *second* step of the final iteration, eqn. (2.7), rather than the *first* step, eqn. (2.6). The magnitude of the anisotropic signal increases in this case to $\sim 30\%$ for the 60 degree mask and $\sim 6\%$ for the 20 degree mask.

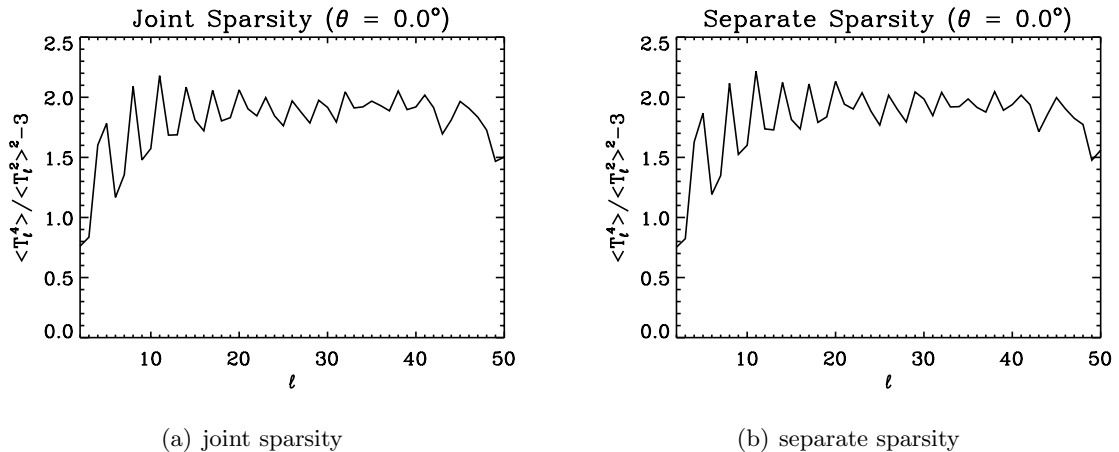


Figure 6. Simulated inpainted trispectrum, evaluated at the North Pole only, for all multipoles up to 50. The results for both joint (left) and separate (right) sparsity indicate that multipoles beyond the octupole are also made anisotropic by the inpainting procedure.

calculating the kurtosis of $a_{\ell 0}$. Recall that the spherical harmonics with $m \neq 0$ are zero at the North Pole, and thus the kurtosis of T_ℓ reduces to the kurtosis of $a_{\ell 0}$ at this position. Fig. 6 shows the kurtosis of $a_{\ell 0}$ for $\ell = 2 - 50$: it is clear from this figure that, for both forms of the sparsity prior, the effect does not vanish at higher ℓ . Again, we leave for future work a complete investigation of these effects under more realistic experimental settings.

5 Conclusions

We have provided analytic computations and simulations suggesting that sparse inpainting techniques using the spherical harmonic dictionary can alter the isotropy properties of Gaussian random fields on the sphere. The effect for a given multipole configuration is around 25% of the Gaussian expected value for a 50% sky cut and remains significant for smaller masks. It must also be kept in mind that the cardinality of different trispectra configurations is extremely high at *Planck* resolution; further investigations are hence needed to assess the cumulative impact for the statistical analysis of a full data set. These issues are beyond the scope of the present paper and left as an avenue for further research, as are investigations into the isotropy properties of sparse inpainting using other dictionaries, such as wavelets.

As noted earlier, our Monte Carlo analysis does not take into account some features of realistic CMB data analysis: in particular, for brevity we focussed on low resolution maps, we did not consider beam and noise effects, and we investigated only partially the effect of a varying width for the masked region. We believe, however, that these technicalities do not affect the basic message of this paper, and we expect that our main theoretical conclusions will remain substantially unaltered under more realistic settings. As previously mentioned, these issues and the relevance of our findings for the analysis of data sets such as those from WMAP [28] and *Planck* are left as topics for future research.

References

- [1] D. Donoho, *Compressed sensing*, *IEEE Trans. Inform. Theory* **52** (apr, 2006) 1289–1306.

- [2] D. L. Donoho, *For most large underdetermined systems of linear equations the minimal 1-norm solution is also the sparsest solution*, *Communications on Pure and Applied Mathematics* **59** (2006), no. 6 797–829.
- [3] R. G. Baraniuk, V. Cevher, and M. B. Wakin, *Low-dimensional models for dimensionality reduction and signal recovery: A geometric perspective*, *Proceedings of the IEEE* **98** (2010), no. 6 959–971.
- [4] E. Candès, J. Romberg, and T. Tao, *Stable signal recovery from incomplete and inaccurate measurements*, *Comm. Pure and Appl. Math.* **59** (Mar., 2006) 1207–1223, [[math/0503](#)].
- [5] H. Rauhut and R. Ward, *Sparse recovery for spherical harmonic expansions*, in *Proc. SampTA*, 2011. [1102.4097](#).
- [6] H. Rauhut and R. Ward, *Sparse Legendre expansions via ℓ_1 minimization*, *Journal of Approximation Theory* **164** (2012), no. 5 517 – 533, [[1003.0251](#)].
- [7] P. Abrial, Y. Moudden, J.-L. Starck, B. Afeyan, J. Bobin, J. Fadili, and M. K. Nguyen, *Morphological component analysis and inpainting on the sphere: application in physics and astrophysics*, *J. Fourier Anal. and Appl.* **14** (2007), no. 6 729–748.
- [8] J.-L. Starck, D. L. Donoho, M. J. Fadili, and A. Rassat, *Sparsity and the Bayesian perspective*, *aap* **552** (Apr., 2013) A133, [[1302.2758](#)].
- [9] J.-L. Starck, M. J. Fadili, and A. Rassat, *Low- ℓ CMB analysis and inpainting*, *Astron. & Astrophys.* **550** (Feb., 2013) A15, [[1210.6587](#)].
- [10] J. D. McEwen, G. Puy, J.-P. Thiran, P. Vandergheynst, D. V. D. Ville, and Y. Wiaux, *Sparse image reconstruction on the sphere: implications of a new sampling theorem*, *IEEE Trans. Image Proc.* **22** (2013), no. 6 2275–2285, [[1205.1013](#)].
- [11] F.-X. Dupé, A. Rassat, J.-L. Starck, and M. J. Fadili, *Measuring the integrated Sachs-Wolfe effect*, *Astron. & Astrophys.* **534** (Oct., 2011) A51, [[1010.2192](#)].
- [12] J.-L. Starck, F. Murtagh, and M. Fadili, *Sparse Image and Signal Processing*. Cambridge University Press, Cambridge, 2010.
- [13] P. Baldi and D. Marinucci, *Some characterizations of the spherical harmonics coefficients for isotropic random fields*, *Statistics and Probability Letters* **77** (2006), no. 5 490–496, [[math/0606](#)].
- [14] P. Baldi, D. Marinucci, and V. S. Varadarajan, *On the characterization of isotropic Gaussian fields on homogeneous spaces of compact groups*, *Electronic Communications in Probability* **12** (2007) 291–302, [[0704.1575](#)].
- [15] D. Marinucci and G. Peccati, *Random Fields on the Sphere: Representations, Limit Theorems and Cosmological Applications*. Cambridge University Press, Cambridge, 2011.
- [16] P. Baldi and S. Trapani, *Fourier coefficients of invariant random fields on homogeneous spaces of compact groups*, *ArXiv e-prints* (Apr., 2013) [[1304.5142](#)].
- [17] R. Gribonval, *Should Penalized Least Squares Regression be Interpreted as Maximum A Posteriori Estimation?*, *IEEE Trans. Sig. Proc.* **59** (May, 2011) 2405–2410.
- [18] B. D. Wandelt, D. L. Larson, and A. Lakshminarayanan, *Global, exact cosmic microwave background data analysis using Gibbs sampling*, *Phys. Rev. D.* **70** (Oct., 2004) 083511, [[astro-ph/](#)].
- [19] J. F. Taylor, M. A. J. Ashdown, and M. P. Hobson, *Fast optimal CMB power spectrum estimation with Hamiltonian sampling*, *Mon. Not. Roy. Astron. Soc.* **389** (Sept., 2008) 1284–1292, [[0708.2989](#)].
- [20] M. Tegmark, *How to make maps from cosmic microwave background data without losing information*, *Astrophys. J. Lett.* **480** (May, 1997) L87, [[astro-ph/](#)].

- [21] S. M. Feeney, H. V. Peiris, and A. Pontzen, *Avoiding bias in reconstructing the largest observable scales from partial-sky data*, *Phys. Rev. D.* **84** (Nov., 2011) 103002, [[1107.5466](#)].
- [22] F. Elsner and B. D. Wandelt, *Fast Wiener filtering of CMB maps*, in *Big Bang, Big Data, Big Computers*, Nov., 2012. [[1211.0585](#)].
- [23] F. Elsner and B. D. Wandelt, *Efficient Wiener filtering without preconditioning*, *Astron. & Astrophys.* **549** (Jan., 2013) A111, [[1210.4931](#)].
- [24] P. Combettes and J.-C. Pesquet, *A douglas-rachford splitting approach to nonsmooth convex variational signal recovery*, *IEEE J. Selected Top. in Sig. Proc.* **1** (dec, 2007) 564–574.
- [25] P. L. Combettes and J.-C. Pesquet, *Proximal Splitting Methods in Signal Processing*, *ArXiv e-prints* (Dec., 2009) [[arXiv:0912.3522](#)].
- [26] D. A. Varshalovich, A. N. Moskalev, and V. K. Khersonskii, *Quantum theory of angular momentum*. World Scientific, Singapore, 1989.
- [27] Planck Collaboration, P. A. R. Ade, N. Aghanim, C. Armitage-Caplan, M. Arnaud, M. Ashdown, F. Atrio-Barandela, J. Aumont, C. Baccigalupi, A. J. Banday, and et al., *Planck 2013 results. I. Overview of products and scientific results*, *ArXiv e-prints* (Mar., 2013) [[arXiv:1303.5062](#)].
- [28] C. L. Bennett, D. Larson, J. L. Weiland, N. Jarosik, G. Hinshaw, N. Odegard, K. M. Smith, R. S. Hill, B. Gold, M. Halpern, E. Komatsu, M. R. Nolte, L. Page, D. N. Spergel, E. Wollack, J. Dunkley, A. Kogut, M. Limon, S. S. Meyer, G. S. Tucker, and E. L. Wright, *Nine-Year Wilkinson Microwave Anisotropy Probe (WMAP) Observations: Final Maps and Results*, *ArXiv e-prints* (Dec., 2012) [[arXiv:1212.5225](#)].
- [29] K. M. Górski, E. Hivon, A. J. Banday, B. D. Wandelt, F. K. Hansen, M. Reinecke, and M. Bartelmann, *HEALPix – a framework for high resolution discretization and fast analysis of data distributed on the sphere*, *Astrophys. J.* **622** (2005) 759–771, [[astro-ph/0409513](#)].

Acknowledgments

We thank Jean-Luc Starck, Mike Hobson, Yves Wiaux, Rémi Gribonval and Mike Davies for useful and lively discussions. SMF is supported by STFC and a grant from the Foundational Questions Institute (FQXi) Fund, a donor-advised fund of the Silicon Valley Community Foundation on the basis of proposal FQXiRFP3-1015 to the Foundational Questions Institute. Research by DM and VC is supported by the European Research Council under the European Community Seventh Framework Programme (FP7/2007-2013) ERC grant agreement no. 277742 *Pascal*. JDM is supported in part by a Newton International Fellowship from the Royal Society and the British Academy. HVP is supported by STFC, the Leverhulme Trust, and the European Research Council under the European Community Seventh Framework Programme (FP7/2007-2013) / ERC grant agreement no. 306478 *CosmicDawn*. BDW is supported by the ANR Chaires d’Excellence programme and NSF grants AST 07-08849 and AST 09-08902 during this work. This work was also supported by ASI/INAF Agreement I/072/09/0 for the *Planck* LFI Activity of Phase E2, French state funds managed by the ANR within the Investissements d’Avenir programme under reference ANR-11-IDEX-0004–02, and by the National Science Foundation under Grant No. PHY11-25915. The authors acknowledge the hospitality of the Big Bang, Big Data, Big Computers workshop at APC, Paris. Some of the results in this paper were derived using the HEALPix package [29].

A The Laplacian trispectrum for the quadrupole and the octupole

In this appendix, we provide some analytic computations to illustrate the anisotropic features which can be introduced by sampling independent, non-Gaussian $a_{\ell m}$ s. It should be noted that we use the prior corresponding to the separate sparsity implementation eqn. (2.4), rather than the joint one in eqn. (2.5). The latter would lead to a different modulation pattern, but it would not alter the message we want to deliver on the existence of anisotropic features. As we have seen in the simulation section, the realized trispectra are very much the same under both optimization schemes.

We make use of several analytic expressions for the spherical harmonics $Y_{\ell m}$ and the associated Legendre functions $P_{\ell m}$; we refer for instance to refs. [15, 26] for further discussion on these functions.

More precisely, we shall focus on the quadrupole $\ell = 2$ and octupole $\ell = 3$, taking for simplicity $\varphi = 0$. For symmetry, we use the real-valued spherical harmonic basis,

$$\{\mathcal{Y}_{\ell m}, m = -\ell, \dots, \ell\} = \left\{ Y_{\ell 0}, \frac{Y_{\ell m} + \bar{Y}_{\ell m}}{\sqrt{2}}, \frac{Y_{\ell m} - \bar{Y}_{\ell m}}{\sqrt{2}i}, m = 1, \dots, \ell \right\},$$

whence we have the equivalence

$$T_{\ell}(\theta, \varphi) = \sum_m a_{\ell m} Y_{\ell m}(\theta, \varphi) = \sum_m \alpha_{\ell m} \mathcal{Y}_{\ell m}.$$

We take the coefficients $\{\alpha_{\ell m}\}$ to be real-valued and Laplacian-distributed with variance unity, so that

$$\mathbb{E}[\alpha_{\ell m}] = \mathbb{E}[\alpha_{\ell m}^3] = 0, \quad \mathbb{E}[\alpha_{\ell m}^2] = 1, \quad \mathbb{E}[\alpha_{\ell m}^4] = 6;$$

in terms of the complex-valued coefficients $\{a_{\ell m}\}$ this entails that

$$\mathbb{E}[a_{\ell 0}] = \mathbb{E}[a_{\ell 0}^3] = 0, \quad \mathbb{E}[a_{\ell 0}^2] = C_{\ell} = 1, \quad \mathbb{E}[a_{\ell 0}^4] = 6,$$

while for $m \neq 0$,

$$\mathbb{E}[a_{\ell m}] = 0, \quad \mathbb{E}[\Re a_{\ell m}]^2 = \mathbb{E}[\Im a_{\ell m}]^2 = \frac{C_{\ell}}{2} = \frac{1}{2}, \quad \mathbb{E}[\Re a_{\ell m}]^4 = \mathbb{E}[\Im a_{\ell m}]^4 = \frac{3}{2},$$

with \Re and \Im denoting as usual real and imaginary parts. Some simple algebra, using the definition and parity properties of spherical harmonics, yields

$$\begin{aligned} T(\theta, \varphi) &= \sum_{\ell=0}^{\infty} \sum_{m=-\ell}^{\ell} a_{\ell m} Y_{\ell m}(\theta, \varphi) \\ &= \sum_{\ell=0}^{\infty} \sum_{m=0}^{\ell} a_{\ell m} Y_{\ell m}(\theta, \varphi) + \sum_{\ell=0}^{\infty} \sum_{m=-\ell}^{-1} a_{\ell m} Y_{\ell m}(\theta, \varphi) \\ &= \sum_{\ell=0}^{\infty} \sum_{m=0}^{\ell} a_{\ell m} Y_{\ell m}(\theta, \varphi) + \sum_{\ell=0}^{\infty} \sum_{m=-\ell}^{-1} (-1)^m \bar{a}_{\ell, -m} (-1)^m \bar{Y}_{\ell, -m}(\theta, \varphi) \\ &= \sum_{\ell=0}^{\infty} \sum_{m=0}^{\ell} a_{\ell m} Y_{\ell m}(\theta, \varphi) + \sum_{\ell=0}^{\infty} \sum_{m=1}^{\ell} \bar{a}_{\ell m} \bar{Y}_{\ell m}(\theta, \varphi) \end{aligned}$$

$$= \sum_{\ell=0}^{\infty} \sum_{m=0}^{\ell} a_{\ell m} \sqrt{\frac{2\ell+1}{4\pi} \frac{(\ell-m)!}{(\ell+m)!}} P_{\ell m}(\cos \theta) e^{im\varphi} + \sum_{\ell=0}^{\infty} \sum_{m=1}^{\ell} \bar{a}_{\ell m} \sqrt{\frac{2\ell+1}{4\pi} \frac{(\ell-m)!}{(\ell+m)!}} P_{\ell m}(\cos \theta) e^{-im\varphi}.$$

Focussing on $\varphi = 0$, we hence obtain

$$\begin{aligned} T(\theta, 0) &= \sum_{\ell=0}^{\infty} \sum_{m=0}^{\ell} a_{\ell m} \sqrt{\frac{2\ell+1}{4\pi} \frac{(\ell-m)!}{(\ell+m)!}} P_{\ell m}(\cos \theta) + \sum_{\ell=0}^{\infty} \sum_{m=1}^{\ell} \bar{a}_{\ell m} \sqrt{\frac{2\ell+1}{4\pi} \frac{(\ell-m)!}{(\ell+m)!}} P_{\ell m}(\cos \theta) \\ &= \sum_{\ell=0}^{\infty} a_{\ell 0} \sqrt{\frac{2\ell+1}{4\pi}} P_{\ell 0}(\cos \theta) + 2 \sum_{\ell=0}^{\infty} \sum_{m=1}^{\ell} \Re a_{\ell m} \sqrt{\frac{2\ell+1}{4\pi} \frac{(\ell-m)!}{(\ell+m)!}} P_{\ell m}(\cos \theta). \end{aligned}$$

For the quadrupole we have that

$$\begin{aligned} T_2(\theta, 0) &:= a_{20} \sqrt{\frac{5}{4\pi}} P_{20}(\cos \theta) + 2 \sum_{m=1}^2 \Re a_{2m} \sqrt{\frac{5}{4\pi} \frac{(2-m)!}{(2+m)!}} P_{2m}(\cos \theta) \\ &= \sqrt{\frac{5}{4\pi}} \left[a_{20} P_{20}(\cos \theta) + 2\Re a_{21} \sqrt{\frac{1}{3!}} P_{21}(\cos \theta) + 2\Re a_{22} \sqrt{\frac{1}{4!}} P_{22}(\cos \theta) \right] \\ &= \sqrt{\frac{5}{4\pi}} \left[\frac{a_{20}}{2} (3 \cos^2 \theta - 1) - 2\Re a_{21} \sqrt{\frac{1}{3!}} 3 \sin \theta \cos \theta + 2\Re a_{22} \sqrt{\frac{1}{4!}} 3 \sin^2 \theta \right] \\ &= \sqrt{\frac{5}{4\pi}} \left[\frac{a_{20}}{2} (3 \cos^2 \theta - 1) - 2\Re a_{21} \sqrt{\frac{3}{2}} \sin \theta \cos \theta + 2\Re a_{22} \sqrt{\frac{3}{8}} \sin^2 \theta \right]. \end{aligned}$$

The standard equality $\mathbb{E}[T_{\ell}^2] = (2\ell+1)C_{\ell}/4\pi = (2\ell+1)/4\pi$ is easily seen to be verified, indeed

$$\begin{aligned} \mathbb{E}[T_2^2(\theta, 0)] &= \frac{5}{4\pi} \mathbb{E} \left[a_{20} P_{20}(\cos \theta) + 2\Re a_{21} \sqrt{\frac{1}{3!}} P_{21}(\cos \theta) + 2\Re a_{22} \sqrt{\frac{1}{4!}} P_{22}(\cos \theta) \right]^2 \\ &= \frac{5}{4\pi} \left[\mathbb{E}[a_{20}^2] P_{20}^2(\cos \theta) + 4\mathbb{E}[(\Re a_{21})^2] \frac{1}{3!} P_{21}^2(\cos \theta) + 4\mathbb{E}[(\Re a_{22})^2] \frac{1}{4!} P_{22}^2(\cos \theta) \right] \\ &= \frac{5}{4\pi} \left[P_{20}^2(\cos \theta) + 4 \frac{1}{2 \cdot 3!} P_{21}^2(\cos \theta) + 4 \frac{1}{2 \cdot 4!} P_{22}^2(\cos \theta) \right] \\ &= \frac{5}{4\pi} \left[\frac{1}{4} (3 \cos^2 \theta - 1)^2 + 4 \frac{1}{2 \cdot 3!} 9 \cos^2 \theta \sin^2 \theta + 4 \frac{1}{2 \cdot 4!} 9 \sin^4 \theta \right] \\ &= \frac{5}{4\pi} \left[\frac{1}{4} (3 \cos^2 \theta - 1)^2 + 3 \cos^2 \theta \sin^2 \theta + \frac{3}{4} \sin^4 \theta \right] \\ &= \frac{5}{4\pi}. \end{aligned}$$

On the other hand, we have

$$\begin{aligned} \mathbb{E}[T_2^4(\theta, 0)] &= \frac{5^2}{4^2 \pi^2} \mathbb{E} \left[a_{20} P_{20}(\cos \theta) + 2(\Re a_{21}) \sqrt{\frac{1}{3!}} P_{21}(\cos \theta) + 2(\Re a_{22}) \sqrt{\frac{1}{4!}} P_{22}(\cos \theta) \right]^4 \\ &= \frac{5^2}{4^2 \pi^2} \left[\mathbb{E}[a_{20}^4] P_{20}^4(\cos \theta) + 2^4 \mathbb{E}[(\Re a_{21})^4] \left(\frac{1}{3!} \right)^2 P_{21}^4(\cos \theta) + 2^4 \mathbb{E}[(\Re a_{22})^4] \left(\frac{1}{4!} \right)^2 P_{22}^4(\cos \theta) \right] \end{aligned}$$

$$\begin{aligned}
& +6\mathbb{E}[a_{20}^2]P_{20}^2(\cos\theta)4\mathbb{E}[(\Re a_{21})^2]\frac{1}{3!}P_{21}^2(\cos\theta) + 6\mathbb{E}[a_{20}^2]P_{20}^2(\cos\theta)4\mathbb{E}[(\Re a_{22})^2]\frac{1}{4!}P_{22}^2(\cos\theta) \\
& +6 \cdot 4\mathbb{E}[(\Re a_{21})^2]\frac{1}{3!}P_{21}^2(\cos\theta)4\mathbb{E}[(\Re a_{22})^2]\frac{1}{4!}P_{22}^2(\cos\theta) \Big] \\
& = \frac{5^2}{4^2\pi^2} \left[6P_{20}^4(\cos\theta) + 2^4\frac{3}{2}\left(\frac{1}{3!}\right)^2 P_{21}^4(\cos\theta) + 2^4\frac{3}{2}\left(\frac{1}{4!}\right)^2 P_{22}^4(\cos\theta) \right. \\
& \quad + 6P_{20}^2(\cos\theta)4\frac{1}{2}\frac{1}{3!}P_{21}^2(\cos\theta) + 6P_{20}^2(\cos\theta)4\frac{1}{2}\frac{1}{4!}P_{22}^2(\cos\theta) \\
& \quad \left. + 6 \cdot 4\frac{1}{2}\frac{1}{3!}P_{21}^2(\cos\theta)4\frac{1}{2}\frac{1}{4!}P_{22}^2(\cos\theta) \right] \\
& = \frac{5^2}{4^2\pi^2} \left[6P_{20}^4(\cos\theta) + \frac{2}{3}P_{21}^4(\cos\theta) + \frac{1}{24}P_{22}^4(\cos\theta) + 2P_{20}^2(\cos\theta)P_{21}^2(\cos\theta) \right. \\
& \quad \left. + \frac{1}{2}P_{20}^2(\cos\theta)P_{22}^2(\cos\theta) + \frac{1}{6}P_{21}^2(\cos\theta)P_{22}^2(\cos\theta) \right] \\
& = \frac{5^2}{4^2\pi^2} \left[\frac{39}{8} - 9\cos^2\theta + \frac{189}{4}\cos^4\theta - 81\cos^6\theta + \frac{351}{8}\cos^8\theta \right]. \tag{A.1}
\end{aligned}$$

Direct substitution of $\cos\theta = 1$ shows that eqn. (3.1) is indeed fulfilled at the North Pole. By an analogous computation, we obtain for the octupole:

$$\begin{aligned}
T_3(\theta, 0) & := a_{30}\sqrt{\frac{7}{4\pi}}P_{30}(\cos\theta) + 2\sum_{m=1}^3(\Re a_{3m})\sqrt{\frac{7}{4\pi}\frac{(3-m)!}{(3+m)!}}P_{3m}(\cos\theta) \\
& = \sqrt{\frac{7}{4\pi}} \left[a_{30}P_{30}(\cos\theta) + 2\sum_{m=1}^3(\Re a_{3m})\sqrt{\frac{(3-m)!}{(3+m)!}}P_{3m}(\cos\theta) \right] \\
& = \sqrt{\frac{7}{4\pi}} \left[a_{30}P_{30}(\cos\theta) + 2(\Re a_{31})\sqrt{\frac{2}{4!}}P_{31}(\cos\theta) + 2(\Re a_{32})\sqrt{\frac{1}{5!}}P_{32}(\cos\theta) + 2(\Re a_{33})\sqrt{\frac{1}{6!}}P_{33}(\cos\theta) \right] \\
& = \sqrt{\frac{7}{4\pi}}\frac{1}{2} \left[a_{30}(5\cos^3\theta - 3\cos\theta) - \sqrt{3}(\Re a_{31})\sin\theta(5\cos^2\theta - 1) + \sqrt{30}(\Re a_{32})\cos\theta\sin^2\theta \right. \\
& \quad \left. + \sqrt{5}(\Re a_{33})\sin^3\theta \right],
\end{aligned}$$

so that, as expected,

$$\begin{aligned}
\mathbb{E}[T_3^2(\theta, 0)] & = \frac{7}{4\pi}\frac{1}{4} \left[(5\cos^3\theta - 3\cos\theta)^2 + \frac{3}{2}\sin^2\theta(5\cos^2\theta - 1)^2 + 15\cos^2\theta\sin^4\theta + \frac{5}{2}\sin^6\theta \right] \\
& = \frac{7}{4\pi},
\end{aligned}$$

and we have

$$\begin{aligned}
\mathbb{E}[T_3^4(\theta, 0)] & = \frac{7^2}{4^2\pi^2}\mathbb{E} \left[a_{30}P_{30}(\cos\theta) + 2(\Re a_{31})\sqrt{\frac{2}{4!}}P_{31}(\cos\theta) + 2(\Re a_{32})\sqrt{\frac{1}{5!}}P_{32}(\cos\theta) \right. \\
& \quad \left. + 2(\Re a_{33})\sqrt{\frac{1}{6!}}P_{33}(\cos\theta) \right]^4
\end{aligned}$$

$$\begin{aligned}
&= \frac{7^2}{4^2\pi^2} \left[\mathbb{E}[a_{30}^4] P_{30}^4(\cos \theta) + 2^4 \mathbb{E}[(\Re a_{31})^4] \frac{2^2}{(4!)^2} P_{31}^4(\cos \theta) + 2^4 \mathbb{E}[(\Re a_{32})^4] \frac{1}{(5!)^2} P_{32}^4(\cos \theta) \right. \\
&\quad + 2^4 \mathbb{E}[(\Re a_{33})^4] \frac{1}{(6!)^2} P_{33}^4(\cos \theta) + 6 \mathbb{E}[a_{30}^2] P_{30}^2(\cos \theta) 2^2 \mathbb{E}[(\Re a_{31})^2] \frac{2}{(4!)} P_{31}^2(\cos \theta) \\
&\quad + 6 \mathbb{E}[a_{30}^2] P_{30}^2(\cos \theta) 2^2 \mathbb{E}[(\Re a_{32})^2] \frac{1}{5!} P_{32}^2(\cos \theta) + 6 \mathbb{E}[a_{30}^2] P_{30}^2(\cos \theta) 2^2 \mathbb{E}[(\Re a_{33})^2] \frac{1}{6!} P_{33}^2(\cos \theta) \\
&\quad + 6 \cdot 2^2 \mathbb{E}[(\Re a_{31})^2] \frac{2}{4!} P_{31}^2(\cos \theta) 2^2 \mathbb{E}[(\Re a_{32})^2] \frac{1}{5!} P_{32}^2(\cos \theta) \\
&\quad + 6 \cdot 2^2 \mathbb{E}[(\Re a_{31})^2] \frac{2}{4!} P_{31}^2(\cos \theta) 2^2 \mathbb{E}[(\Re a_{33})^2] \frac{1}{6!} P_{33}^2(\cos \theta) \\
&\quad \left. + 6 \cdot 2^2 \mathbb{E}[(\Re a_{32})^2] \frac{1}{5!} P_{32}^2(\cos \theta) 2^2 \mathbb{E}[(\Re a_{33})^2] \frac{1}{6!} P_{33}^2(\cos \theta) \right] \\
&= \frac{7^2}{4^2\pi^2} \left[6 P_{30}^4(\cos \theta) + 2^4 \frac{3}{2} \frac{2^2}{(4!)^2} P_{31}^4(\cos \theta) + 2^4 \frac{3}{2} \frac{1}{(5!)^2} P_{32}^4(\cos \theta) \right. \\
&\quad + 2^4 \frac{3}{2} \frac{1}{(6!)^2} P_{33}^4(\cos \theta) + 6 P_{30}^2(\cos \theta) 2^2 \frac{1}{2} \frac{2}{(4!)} P_{31}^2(\cos \theta) \\
&\quad + 6 P_{30}^2(\cos \theta) 2^2 \frac{1}{2} \frac{1}{5!} P_{32}^2(\cos \theta) + 6 P_{30}^2(\cos \theta) 2^2 \frac{1}{2} \frac{1}{6!} P_{33}^2(\cos \theta) \\
&\quad + 6 \cdot 2^2 \frac{1}{2} \frac{2}{4!} P_{31}^2(\cos \theta) 2^2 \frac{1}{2} \frac{1}{5!} P_{32}^2(\cos \theta) + 6 \cdot 2^2 \frac{1}{2} \frac{2}{4!} P_{31}^2(\cos \theta) 2^2 \frac{1}{2} \frac{1}{6!} P_{33}^2(\cos \theta) \\
&\quad \left. + 6 \cdot 2^2 \frac{1}{2} \frac{1}{5!} P_{32}^2(\cos \theta) 2^2 \frac{1}{2} \frac{1}{6!} P_{33}^2(\cos \theta) \right] \\
&= \frac{7^2}{4^2\pi^2} \left[6 P_{30}^4(\cos \theta) + \frac{1}{6} P_{31}^4(\cos \theta) + \frac{4!}{(5!)^2} P_{32}^4(\cos \theta) \right. \\
&\quad + \frac{4!}{(6!)^2} P_{33}^4(\cos \theta) + P_{30}^2(\cos \theta) P_{31}^2(\cos \theta) \\
&\quad + \frac{1}{10} P_{30}^2(\cos \theta) P_{32}^2(\cos \theta) + \frac{1}{60} P_{30}^2(\cos \theta) P_{33}^2(\cos \theta) \\
&\quad + \frac{1}{60} P_{31}^2(\cos \theta) P_{32}^2(\cos \theta) + \frac{2}{6!} P_{31}^2(\cos \theta) P_{33}^2(\cos \theta) \\
&\quad \left. + \frac{1}{5 \cdot 6!} P_{32}^2(\cos \theta) P_{33}^2(\cos \theta) \right] \\
&= \frac{7^2}{4^2\pi^2} \left[\frac{147}{32} - \frac{261}{16} \cos^2 \theta + \frac{4977}{32} \cos^4 \theta - \frac{5115}{8} \cos^6 \theta + \frac{40725}{32} \cos^8 \theta - \frac{19125}{16} \cos^{10} \theta \right. \\
&\quad \left. + \frac{13575}{32} \cos^{12} \theta \right]. \tag{A.2}
\end{aligned}$$

Once again, direct substitution of $\cos \theta = 1$ shows that eqn. (3.1) is indeed fulfilled at the North Pole. Note that obtaining a polynomial in $\cos \theta$ of degree 12 is expected, as $T_\ell(\theta, \varphi)$ is a cubic polynomial in $\cos \theta$ when $\varphi = 0$. The expressions for the quadrupole and the octupole are plotted in Fig. 2 of Sect. 4.